Quantifying Eulerian Eddy Leakiness in An Idealized Model

Tongya Liu[1,2], Ryan Abernathey[3], Anirban Sinha[4], and Dake Chen[2]

[1]Ocean college, Zhejiang University, Zhoushan, Zhejiang, China
[2]State Key Laboratory of Satellite Ocean Environment Dynamics, Second Institute of Oceanography, Ministry of Natural Resources, Hangzhou, Zhejiang, China
[3]Lamont-Doherty Earth Observatory, Columbia University, New York, NY, USA
[4]California Institute of Technology, Pasadena, CA, USA

Key Points:

- SSH eddies overestimate coherent core and fail to reveal more than half of Lagrangian eddies
- The leakage of SSH eddies reach more than 50% over the lifetime
- About half of SSH eddies are not significantly different from random ocean pieces in material coherence

Corresponding author: Tongya Liu, liutongya@sio.org.cn

Abstract

An idealized eddy-resolving ocean basin, closely resembling the North Pacific ocean, is simulated using MITgcm. We identify rotationally coherent Lagrangian vortices (RCLVs) and sea surface height (SSH) eddies based on the Lagrangian and Eulerian framework, respectively. General statistical results show that RCLVs have a much smaller coherent core than SSH eddies with the ratio of radius is about 0.5. RCLVs are often enclosed by SSHA contours, but SSH eddy identification method fails to detect more than half of RCLVs. Based on their locations, two types of eddies are classified into three categories: overlapping RCLVs and SSH eddies, non-overlapping SSH eddies, and non-overlapping RCLVs. Using Lagrangian particles, we examine the processes of leakage and intrusion around SSH eddies. For overlapping SSH eddies, over the lifetime, the material coherent core only accounts for about 25%, and about 50% of initial water leak from eddy interior. The remaining 25% of water can still remain inside the boundary, but only in the form of filaments outside the coherent core. For non-overlapping SSH eddies, more water leakage (about 60%) occurs at a faster rate. Following the number and radius of real SSH eddies, fixed circles and moving circles are randomly selected to diagnose the material flux around these circles. We find that the leakage and intrusion trends of moving circles are quite similar to that of non-overlapping SSH eddies, suggesting that the material coherence properties of non-overlapping SSH eddies are not significantly different from random pieces of ocean with the same size.

Plain Language Summary

Material coherent transport is widely estimated based on the Eulerian methods, but the organization of Eulerian eddies determines Eulerian eddies can not keep material coherence during the lifespan. In this study, we examine the relationship between eddy detection methods and material coherent transport, and quantitatively estimate the Eulerian eddy leakiness in material transport. We compare the statistical features of RCLVs and SSH eddies identified from a high-resolution idealized model based on two different frameworks. We find that the Eulerian method fails to detect many Lagrangian structures and overestimate the real coherent core. Besides, using Lagrangian particles, we quantify the material flux across SSH eddies boundaries. Our results suggest that SSH eddies are far from coherent structures, with the leakage of initial water reach at least 50%. We also find that one type of SSH eddies are not significantly different from random pieces of ocean with the same size in material coherence properties. Our findings suggest that using Eulerian eddy boundaries to estimate coherent transport may be misleading.

1 Introduction

Mesoscale eddies with horizontal spatial scales broadly between tens and a few hundred kilometers are ubiquitous structures in the ocean (*Fu et al.* [2010]), transporting and redistributing mass, heat, salt, potential vorticity, and other biochemical tracers throughout the ocean. This transport is believed to have significant impacts on the large-scale ocean circulation, marine ecosystems, and long-term earth climate (e.g. *Jayne and Marotzke* [2001]; *Dong et al.* [2014]; *Zhang et al.* [2014]; *Gaube et al.* [2015]; *Griffies et al.* [2015]; *Kouketsu et al.* [2016]). Understanding the degree of coherent eddy transport is a key issue for more accurate parameterization of mesoscale transport in coarse-resolution climate models. Here "coherent eddy transport" refers to the water trapping process, in which material transport barriers prevent effective water exchange between the eddy interior and background flows over a finite time interval (*Frenger et al.* [2015]; *Haller and Beron-Vera* [2013]; *Haller* [2015]). However, a survey of previous studies reveals that estimates of coherent eddy transport based on different identification methods vary dramatically. In this paper, we aim to clarify the relationship between eddy identification methods and material coherent transport. Also, we seek to examine the extent to which the eddies detected by different methods maintain coherence over their lifetimes.

A number of methods have been employed to identify coherent eddies. We review these methods in two categories: Eulerian methods, based on instantaneous information of the flow

field, and Lagrangian methods, based on water parcel trajectories over a finite time interval. The fundamental concept of Eulerian methods is to identify the eddy boundary through anomaly contours of some instantaneous Eulerian field, and then track these boundaries on the basis of their geographic locations at a proximate time. The Eulerian fields used to define the ocean eddy boundaries include OkuboWeiss (OW) parameter (*Okubo* [1970]; *Weiss* [1991]; *Isern-Fontanet et al.* [2003]), sea surface height (SSH; *Chelton et al.* [2011]; *Faghmous et al.* [2015]), velocity streamlines (*Nencioli et al.* [2010]), sea surface temperature (*Dong et al.* [2011]; *Hausmann and Czaja* [2012]), and potential vorticity (*Zhang et al.* [2014]). Due to their relative computational simplicity, the Eulerian methods have been more widely used in the oceanography community, especially the eddy census of *Chelton et al.* [2011] derived from satellite altimetry.

Eulerian eddy detection has many valuable applications. However, several shortcomings of Eulerian detection methods (discussed by *Haller* [2015] and *Peacock et al.* [2015]) must be considered in the context of eddy transport. First, the Eulerian methods are not objective; material transport should not depend on the choice of reference frame, but Eulerian eddies may change dramatically when the reference frame changes (e.g. via translation or rotation). Second, the boundary of the Eulerian eddy is not material; the contours in scalar field do not represent persistent material barriers that forbid material exchange. That means the water inside Eulerian eddy boundaries is not necessarily the same fluid at different times. In addition, the choice of numerous parameters and thresholds is another inevitable drawback of Eulerian methods. In contrast, Lagrangian coherent structures derived from Lagrangian fluid motion are a natural choice for assessing coherent eddy transport, since they are material by construction. Recently, several different methods, including finite-time Lyapunov exponents (FTLE; *Beron-Vera et al.* [2008]), finite-scale Lyapunov exponent (FSLE; *dÓvidio et al.* [2009]), geodesic transport barriers (*Haller and Beron-Vera* [2013]; *Beron-Vera et al.* [2013, 2015]), and Lagrangian-averaged vorticity deviation (LAVD; *Haller et al.* [2016]), have been introduced to reveal materially coherent ocean eddies.

Among numerous studies to estimate material coherent transport based on Eulerian identification methods, the following two have received considerable attention due to their global scope and surprising results. Under the framework of Eulerian eddy detection, *Dong et al.* [2014] combined Argo profile data and a velocity-based Euerian eddy dataset to estimate horizontal heat and salt transports due to coherent eddy translation. They concluded that most of the eddy transport in the ocean is due to individual eddy movements. *Zhang et al.* [2014] defined the eddy boundary via the outermost closed potential vorticity contour and conducted a similar calculation for eddy mass transport. They found that the zonal westward mass flux induced by eddies in the subtropical gyres can reach about 30 Sv, which is comparable to the wind-driven transport.

However, several works using Lagrangian frameworks have presented quite conflicting results. For instance, *Abernathey and Haller* [2018] adopted the Lagrangian-averaged vorticity deviation method of *Haller et al.* [2016] to detect eddies in the eastern Pacific and quantified the contribution of coherent transport to total transport. They found that the coherent meridional transport accounted for less than 1% of the total flux, and the incoherent part, including chaotic stirring and filamentation outside of eddy cores, was the dominant mechanism for eddy transport. Similarly, the work of *Beron-Vera et al.* [2013], *Froyland et al.* [2015]) and *Wang et al.* [2015, 2016] examined the ability of Agulhas rings to coherently carry Agulhas leakage water using Lagrangian methods, finding considerably smaller transport estimates than previous Eulerian-based methods. Most recently, *Cetina-Heredia et al.* [2019] quantified the time that mesoscale eddies along the southeast coast of Australia retain water and pointed out the change in eddy shape relates to water exchange between the eddy interior and the background flow. Though Eulerian eddies can temporarily trap and transport water parcels and tracers (*Gaube et al.* [2015]; *Condie and Condie* [2016]), under the effects of stretching and filamentation, such eddies may lose coherence and experience leakage and deformation in the turbulent flow(*Haller* [2005]; *Early et al.* [2011]. The Lagrangian frameworks suggest that the coherent material transport is very limited in the ocean, and that Eulerian-based estimates of transport with strong assumptions about material coherence need revision. A systematic quantification of the Eulerian eddy leakiness over their full lifespan has, to our knowledge, not yet been attempted.

The main goal of this study is to answer the following key issues: (1) What are the differences between Eulerian and Lagrangian eddies in terms of coherent transport? (2) How leaky are Eulerian eddies over their lifetime? We choose rotationally coherent Lagrangian vortices (RCLVs) and sea surface height (SSH) eddies as the representative of Lagrangian eddies and Eulerian eddies in this study. The paper is organized as follows. In Section 2, we present a brief description of the idealized eddy-resolving model and two different coherent eddy identification methods. In Section 3, we compare general statistical features of Lagrangian eddies to those of Eulerian eddies. In Section 4, we examine the material flux across SSH eddy boundaries. Section 5 describes the material flux for random-circle eddy model, as a baseline for comparison against the SSH eddies. Discussion and conclusions are shown in Section 6.

2 Methods

2.1 Description of idealized model

Our goal is to create an eddy-resolving simulation which produces materially coherent eddies with characteristics and spatial variability broadly similar to those of the real ocean. Because a past study focused on the Pacific basin *Abernathey and Haller* [2018], here we create an idealized Pacific-like scenario. The Massachusetts Institute of Technology general circulation model (MITgcm; *Marshall et al.* [1997a,b]) is employed to construct an eddy-resolving idealized model with a 0.1 degree resolution. This resolution is adopted by many state-of-the-art global climate models (e.g. GFDL CM2.6) and it allows the model to resolve the deformation radius with least 2 grid points at about 40 ° N. North of this latitude is must be considered eddy permitting (*Hallberg* [2013]). The model domain (shown in Fig. 1d) is a rectangular basin spanning 144 degrees in longitude and 60 degrees in latitude. It is bounded by simple land masses along the western and eastern boundary, closely approximating the topography of the North Pacific, which is motivated by the model of *Cox* [1985]. A no-slip condition is imposed at four solid boundaries. The basin bottom is flat and 4000 m deep, except for a continental shelf along the western boundary, obeying an exponential profile from 200 m at the land to 4000 m in 4 degrees to the east of the land. Vertically, there are 29 unevenly spaced layers, ranging from 10 m at the surface to 500 m at the bottom.

The surface forcing in the model consists of zonally uniform zonal wind stress and surface temperature relaxation. The wind stress profile is based on zonally averaged zonal wind stress over the North Pacific from QuikSCAT (*Risien and Chelton* [2008]). The surface temperature relaxation forcing is described as a linear function of latitude only, with the value decrease from 30°C at the equator to 5°C at 60° N. The relaxation time scale is 1 month. The distributions of wind stress and surface temperature forcing are shown in Figure 1 (a) and (b). In order to maintain the vertical stratification in the tropical region, we introduce a narrow sponge layer along the southern boundary, in which the temperature is relaxed to prescribed stratification profile from World Ocean Atlas 2013 (https://www.nodc.noaa.gov/OC5/woa13/woa-info.html) with a time scale of one month. For the sake of model simplicity, a linear equation of state is adopted and the salinity equation is turned off. The nonlocal K-profile parametrization (KPP; *Large et al.* [1994]) is used to parameterize vertical mixing in the surface boundary layer, and the Modified Leith Visosity (*Fox-Kemper and Menemenlis* [2008]) is adopted for numerical viscosity. Full details about the physical and numerical parameters used in the model and a reproducible configuration are available at https://github.com/liutongya/Box_model.

The model run consists of three stages. In the first stage, a coarse grid model with a 1 degree resolution is integrated for 300 years, whereupon a near steady state circulation is obtained indicated by the mean kinetic energy. Then the 0.1 degree model is initialized at this point via interpolation and integrated for 100 years to generate the circulation brimming with eddies. Finally, the Lagrangian particle advection and eddy identification is conducted on the basis of the eddy-resolving solution for another 5 years.

Climatological averages are calculated over the last 50 years and are used to assess this idealized solution via comparisons with previous literature and observations of gyre structure, vertical stratification, and eddy kinetic energy (EKE) distribution. As shown in Figure 1 (d), the uniform zonal

wind stress generates a double gyre circulation, with a strong concentrated eastward flow (like the Kuroshio extension) between the subtropical and subpolar gyres. The pattern of sea surface height (SSH) is quite comparable to mean dynamic topography derived from satellite and in situ data (see Figure 3 in *Rio et al.* [2011]). The latitude-depth section of temperature along 15° E (approximately equivalent to 137° E in real ocean) is shown in Figure 1 (c, black contours), together with zonal velocity expressed by colors. The model captures the main features of thermal structures and banded flows in tropical and subtropical regions reflected by hydrographic surveys in *Qiu and Chen* [2010] (Figure 2). That is, the main thermocline (taking the 10° C isotherm) deepens strongly with latitude in the subtropical interior, and then upraises suddenly at about 32° N. In addition, the comparison of EKE distributions between AVISO data and model result indicates the model properly reproduces two eddy bands in the subtropical circulation, with one band located in Kuroshio extension region and another one located in the North Equatorial Current (NEC) region. A supplementary animation of daily SST in the final year is available at https://vimeo.com/341264533.

Overall, the idealized model well simulates the general wind-driven circulation with strong eddy activity in the upper ocean. This simulation is a computationally efficient way to probe eddy dynamics at a resolution similar to contemporary state-of-the-art high-resolution global climate models. Based on the results of *Sinha et al.* [2019], we expect that higher resolution would probably lead to fewer coherent eddies, due to the emergence of submesoscale structures at mesoscale eddy boundaries, but we do not purse the question of resolution dependence here.

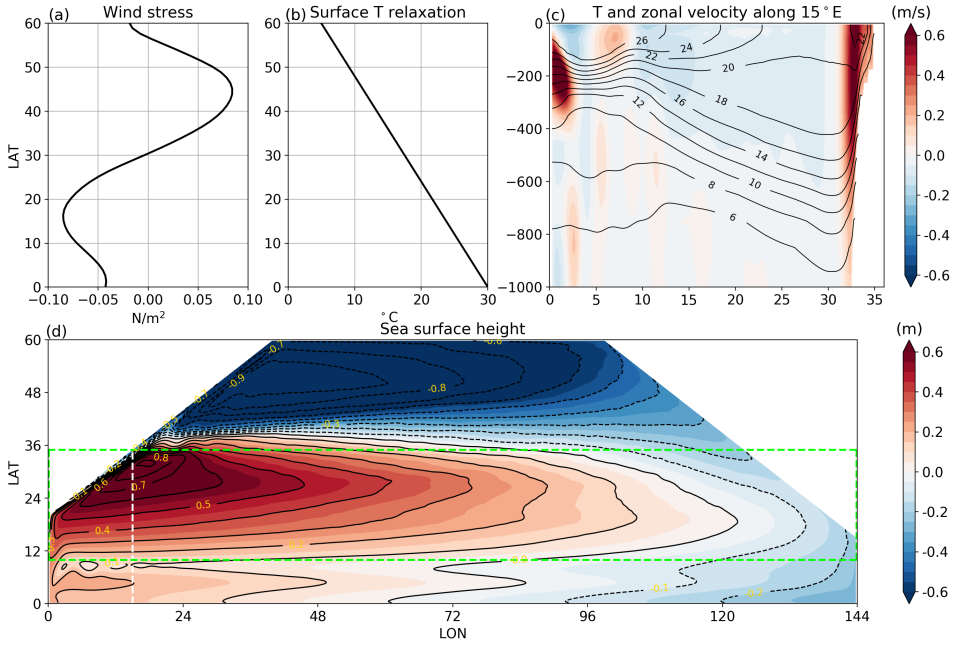

Figure 1. Model forcing fields and climatological results. (a) wind stress, (b) relaxation temperature, (c) temperature (black contours) and zonal velocity (colors) profile along 15 °E, and (d) sea surface height. The white dashed line is the profile for (c). The green dashed line box is the region for eddy identification.

2.2 Identification of Lagrangian and Eulerian eddies

In the final 5 years, the Lagrangian particles are initialized with uniform spacing of 1/80 ° on the surface covering the whole domain, with more than 55 million points. As described in *Haller et al.* [2016] and *Abernathey and Haller* [2018], a dense mesh of Lagrangian particles, much higher resolution than the model grid itself, is necessary to reflect the fine structure of transport barriers and properly identify Lagrangian eddies. The particles can be advected for 90 days by 2D surface flow

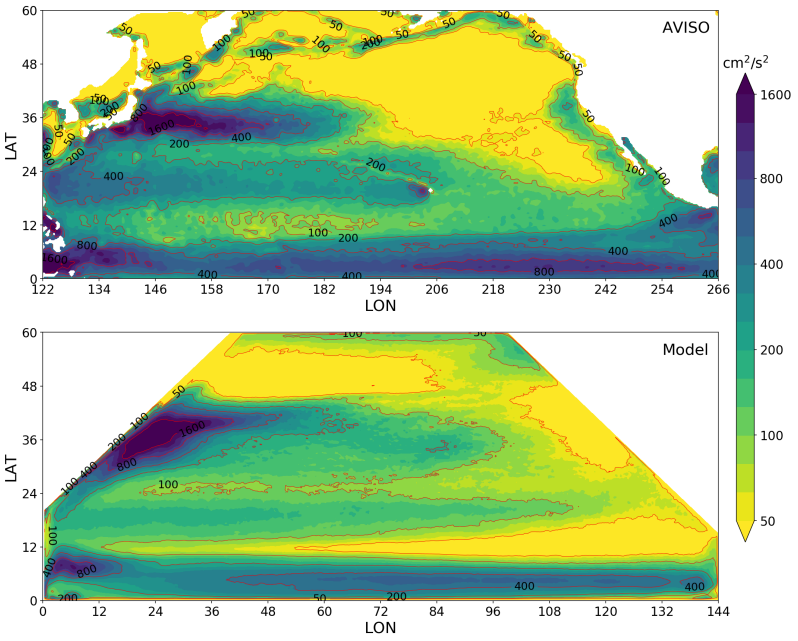

Figure 2. Comparison of EKE fields from (upper) AVISO and (bottom) model.

in "online mode" till the next initialization. In the following analysis, we use 20 non-overlapping 90-day time intervals in total for identifying eddies. In this paper our focus is on the near-surface horizontal flow, and consequently our particles are advected by the surface flow only (top model vertical level). Such trajectories are thus most representative of buoyant material such as marine debris or pollutants. However, due to the relatively low Rossby number and consequently weak divergence in the 2D flow, these trajectories are reasonably close to full 3D trajectories. (This was confirmed by full 3D advection tests.) A future study in preparation will examine the 3D structure of material eddies in this simulation.

Our definition of a Lagrangian eddy, one of many possible choices, is based on the concept of coherent rotation. Over its lifetime, all water parcels along a coherent eddy boundary should have the same average angular speed when rotating around the eddy core, in analogy to rigid-body rotation,. Based on this physical concept, *Haller et al.* [2016] proposed that the material boundary of a rotationally coherent Lagrangian vortex (RCLV, also called Lagrangian eddy) can be found by identifying the outermost closed contours of the Lagrangian-averaged vorticity deviation (LAVD, adopted by *Abernathey and Haller* [2018]; *Tarshish et al.* [2018]; *Sinha et al.* [2019]).

In a two dimensional flow, given a finite time interval (t_0, t_1), LAVD is defined as the average of the vorticity deviation along the Lagrangian particle trajectory, that is,

$$LAVD_{t_0}^{t_1}(x_0, y_0) = \frac{1}{t_1 - t_0} \int_{t_0}^{t_1} |\zeta'[X(x_0, y_0, t), Y(x_0, y_0, t), t]|\, dt. \tag{1}$$

Where (X, Y) denotes the position for the particle initially located in point (x_0, y_0) and ζ' indicates the instantaneous relative vorticity deviation from the spatial average over the whole domain. LAVD reflects the average magnitude of local rotation for each Lagrangian particle over the time interval. The Lagrangian view makes it essentially different from Eulerian detection methods, for instance, defining coherent eddies by instantaneous vorticity contours. The local maximum of the LAVD field (corresponding to the strongest local rotation) represents the Lagrangian vortex center, and the vortex boundary is the outermost closed LAVD curve encircling the center.

Any closed curve of the LAVD field is a plausible, objective choice for the Lagrangian eddy boundary. To constrain our choice of boundary, we employ two additional heuristics. Convexity deficiency (CD), defined by *Haller et al.* [2016], describes how strongly the boundary curve departs from a convex curve. Coherency index (CI), introduced by *Tarshish et al.* [2018], measures how much the particles within the eddy disperse away from the eddy center. Starting from a local maximum of LAVD, we search outward for the closed LAVD contour using a bisection search algorithm, until we obtain the outermost contour satisfying both CD and CI thresholds. In this study, we choose threshold values of CD=0.1 and CI=-2, which are reasonable conditions for RCLV detection according to the sensitivity analysis in *Tarshish et al.* [2018]. We have integrated the LAVD detection method into an open source Python package named `floater` available at https://github.com/rabernat/floater.

The method we use to detect and track SSH eddies is described in *Faghmous et al.* [2015]. This geometric eddy identification method is very similar to that proposed by *Chelton et al.* [2011] and detects mesoscale eddies based on closed contours of SSH anomaly (SSHA) data. Similar to *Chelton et al.* [2011], they published a global daily mesoscale ocean eddy map over a period of 1993-2004 from the AVISO dataset. However, *Faghmous et al.* [2015] developed an open source MATLAB code which can be applied to reproduce their detection algorithm and apply it to new scenarios. The algorithm is available at https://github.com/jfaghm/OceanEddies. We used this code to detect Eulerian eddies in our model.

3 Census of Lagrangian vortices and Eulerian eddies

3.1 Quantity statistics of eddies

In the subtropical region (green dashed line box shown in Figure 1d), the LAVD method and SSH contour method are applied to identify RCLVs and SSH eddies in 20 90-day time intervals. Compared to SSH eddies, the most peculiar thing about RCLVs is that they are identified on specific time intervals. In this case, we initialize the detection at the first day of each 90-day time interval and then identify 30-, and 90-day RCLVs from that initialization date. For SSH eddies, the identification is carried out continuously in 5 years and the complete SSH eddy dataset is obtained. To compare RCLVs and SSH eddies in the same time interval, we extract SSH eddies from the complete dataset, by the condition that the SSH eddy has existed on the RCLV initialization time and can last for more than 30 and 90 days from that date. The eddies with the radius less than 25 km are excluded.

In Figure 3, we randomly choose a small region (40 °-70 °E & 12 °-26 ° N) to show the initial locations of detected 30-day RCLVs and SSH eddies with lifespans longer than 30 days, with the SSHA field superimposed. Based on whether there is a RCLV whose center is located within the boundary of a SSH eddy, all eddies can be classified into three categories: overlapping RCLVs and SSH eddies, non-overlapping SSH eddies, and non-overlapping RCLVs. For overlapping RCLVs and SSH eddies, one notable character is that the RCLVs have a much smaller area than that of the corresponding SSH eddy and are enclosed by SSHA contours, which is consistent with the results of *Abernathey and Haller* [2018]. For non-overlapping SSH eddies, though they are identified and tracked by Eulerian detection algorithm, they do not maintain material coherence over the detection time interval. For example, an Eulerian eddy with with a large SSHA amplitude (such as the one located in about 63 ° E & 24 ° N) appears to be a eddy, but our result in section 4 illustrate that this kind of eddy may not be a materially coherent structure. Conversely, the non-overlapping RCLVs are the Lagrangian structures that SSH contour algorithm fails to identify. Among non-overlapping RCLVs, there are a fraction of vortices (about 25% of total RCLVs) that are not located nearby the local peak of SSHA. They are quite different from the classic geostrophic eddy centered on an SSHA extremum, but they are indeed materially coherent as indicated by LAVD method. Here we mainly focus on examining the leakiness of SSH eddies, so we will not discuss the details of these special RCLVs in this paper. The statistics presented below confirm that these results are typical rather than anomalous.

The statistics for the total numbers of RCLVs and SSH eddies are shown in Figure 4. We identify 5412 RCLVs and 4144 SSH eddies (extracted from the complete dataset) with lifetimes $\geqslant$30

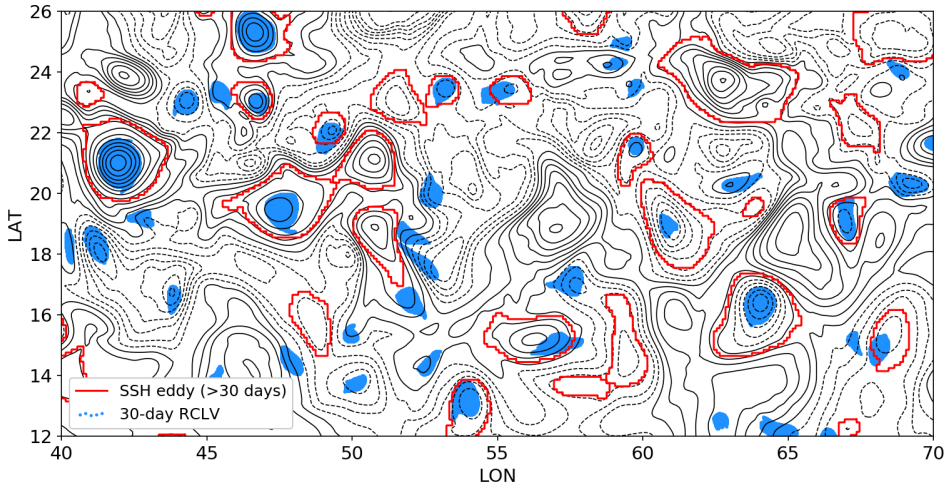

Figure 3. The initial locations of 30-day RCLVs and SSH eddies (>30 days) in a randomly selected time interval and region. The blue dots present particles within each RCLV boundary. The red lines denote SSH eddy boundaries. The SSHA contours are shown in black solid and dashed lines, with the contour interval of 1 cm.

days in subtropical region over five years. The numbers of 30-day RCLVs in each 90-day interval fluctuates between 250 and 300, The longer-lived vortices are rare, with about 70 in each interval for 90-day RCLVs. A similar ratio of >90 days eddies to >30 day eddies (1/5) is found in SSH eddies. Another interesting observation is that the total number of SSH eddies is slightly less than that of RCLVs, since non-overlapping RCLVs are the most numerous type.

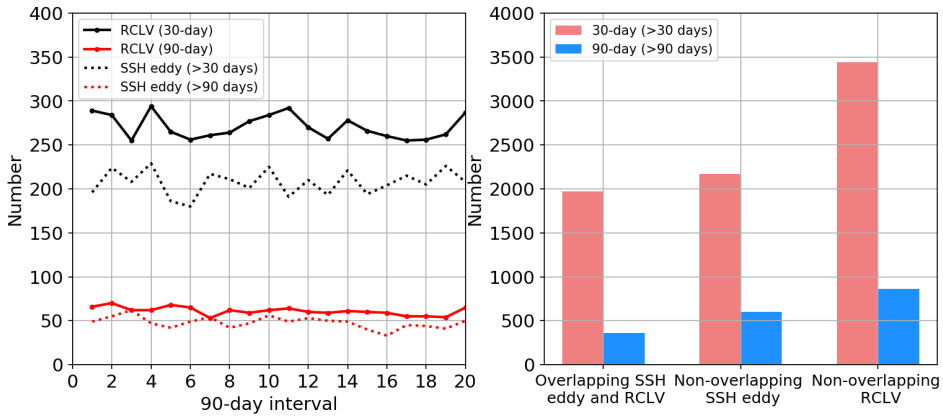

Figure 4. RCLVs and SSH eddies number statistics. (left) Time series of RCLVs and SSH eddies number in 20 90-day intervals. (right) Total numbers of overlapping SSH eddies and RCLVs, non-overlapping SSH eddies, and non-overlapping RCLVs. The colors correspond to the eddy lifespans in both two panels.

3.2 Radius, propagation speed, and zonal coherent transport

The equivalent radius R of RCLVs and SSH eddies is converted from the eddy horizontal area A by the formula $R = \sqrt{A/\pi}$. We also calculate the first Rossby radius of deformation L_d via

$$L_d = \frac{1}{f\pi}\int_{-H}^{0} N(z)dz, \tag{2}$$

where, f is the Coriolis parameter for earth rotation and latitude, H is the water depth, and $N(z)$ is the buoyancy frequency obtained from model vertical stratification.

The top two panels in Figure 5 show the comparison of radius for 30-day RCLVs and SSH eddies with lifetimes longer than 30 days. A box-and-whisker plot represents statistics of all eddies in 2.5° latitude bins. With the increase of Coriolis parameter, the first Rossby deformation radius (purple dashed lines) decreases from about 95 km at 10° N to about 25 km at 35° N, which is similar to the distribution in *Chelton et al.* [1998]. Comparing with SSH eddies, the mean RCLV radius (35.5 km) is approximately about half of the mean SSH eddy radius (72.4 km). In contrast with *Abernathey and Haller* [2018], no significant latitude dependence or relationship with deformation radius is visible in either RCLVs or SSH eddies. The SSH eddy radii of about 60 km in the low latitudes (about 10° N) are smaller than the observation (more than 100 km). The relative lower eddy activity in the region around 10° N (Figure 2) indicates our model may fail to generate realistic eddies in the tropics, likely caused by biases in the model background state. Most of our focus in what follows is on the midlatitudes.

The zonal propagation speed c of RCLVs and SSH eddies, derived from the zonal displacement over the lifetime, is shown in the bottom two panels of Figure 5. We observe RCLVs and SSH eddies have similar westward propagation speeds at each latitude in the subtropical region, nearly consistent with the phase speed of nondispersive long-wave Rossby wave (also captured by the result based on AVISO data in *Abernathey and Haller* [2018]) except for the low latitude region. The phase speed c_p is calculated by

$$c_p = \bar{U} - \beta L_d^2, \tag{3}$$

where, $\bar{U}$ is the depth-averaged zonal flow (*Klocker and Marshall* [2014]).

Having obtained radius and zonal propagation speed of eddies, we now can estimate the advective material transport by coherent eddy movement following the methods proposed by *Dong et al.* [2014] and *Zhang et al.* [2014] These methods assume Eulerian eddy is materially coherent, trapping its interior water parcels and translating them uniformly without water exchange with the surrounding environment. (This is true by construction for RCLVs.) Here we temporarily assume SSH eddies can are materially coherent in order to make this calculation, despite evidence to the contrary. The vertical depth and structure of coherent eddies is still an open issue; therefore, to avoid artificially introducing the depth of eddies, we define cross-longitude transport by $Q = cL_{yz} = 2Rc$, with units of m^2/s. Figure 6 shows the zonally averaged zonal transport per degree latitude averaged over 5 years for 30- and 90-day eddies. The coherent transport of RCLVs is uniformly smaller than that of SSH eddies at each latitude, since the coherent core of RCLVs is only half of SSH eddy radius, applying to both 30- and 90-day eddies. If the constant vertical depth 500 m is used to compute volume transport, the peak value of the zonal advective transport for 30-day RCLVs is about 0.3 Sv, much weaker than the estimate larger than 1 Sv in the Pacific ocean by *Zhang et al.* [2014] (see their Figure 3).

These statistical results suggest that, the RCLVs and SSH eddies move at the similar speed, and the zonal coherent transport by RCLVs is around half of the transport by SSH eddies due to large coherent core defined by SSH contours. However, this is not the case; the next section shows that the SSH eddies are far from materially coherent structures.

4 Material Flux Across Eddy Boundaries

The RCLVs are materially coherent by construction, but the material coherence properties of the SSH eddies require investigation. Having described the statistics of Lagrangian vortices and Eulerian eddies, we now focus on the core issue of our study: how leaky are the Eulerian eddies in terms of material transport?

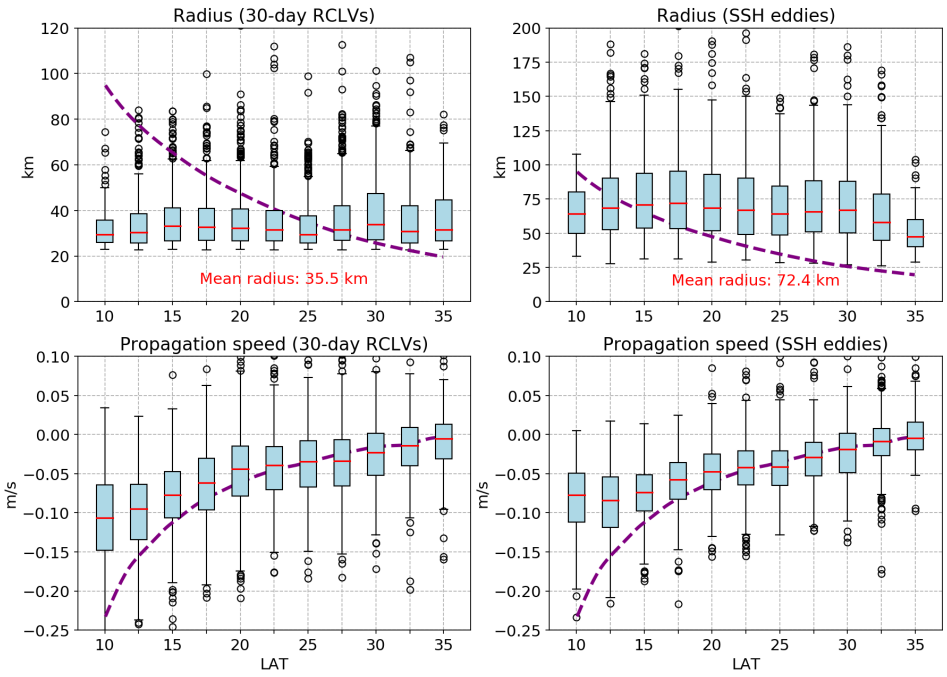

Figure 5. (top) Radius and (bottom) propagation speed statistics of (left) 30-day RCLVs and (right) >30 days SSH eddies. A box-and-whisker plot shows statistics of all eddies in 2.5 bins. The red line represents the median. The blue box covers 25th-75th percentiles of the distribution. The black whiskers indicate 5th-95th percentiles. The black circle symbols represent the outliers beyond 5th-95th percentiles. The purple dashed line in top two panels is zonally averaged first baroclinic Rossby radius of deformation in kilometers. Mean radii of RCLVs and SSH eddies (labeled in red text) are 35.5 km and 72.4 km, respectively.

4.1 Reynolds transport theorem

For a conserved scalar ϕ (e.g. conservative temperature for heat transfer) without source and sink in a Boussinesq flow, the conservation equation is given by,

$$\frac{\partial \phi}{\partial t} + \vec{u} \cdot \nabla \phi = 0. \tag{4}$$

Here, $\vec{u}$ is the velocity vector field. Consider a 2-D mesoscale eddy system and a coinciding control surface Ω with a control boundary $\partial\Omega$, according to Reynolds transport theorem (*Reynolds et al.* [1903]), the time derivative of integrated ϕ over the eddy system is determined by the time rate of change of ϕ within the control eddy surface and the net rate of flux of ϕ through the moving eddy boundary,

$$\frac{d}{dt}\int_{\Omega} \phi dA = \int_{\Omega} \frac{\partial \phi}{\partial t} dA + \oint_{\partial\Omega} \phi \vec{u_b} \cdot \hat{n} dS. \tag{5}$$

Where, dA and dS are area and line elements, u_b is the velocity of eddy boundary, and $\hat{n}$ is the outward-pointing unit normal vector. The definition of a material region is that the boundary velocity $\vec{u_b}$ equals the fluid velocity $\vec{u}$. Combining Gauss's theorem and (3), (4) Reynold's transport theorem for a material eddy becomes

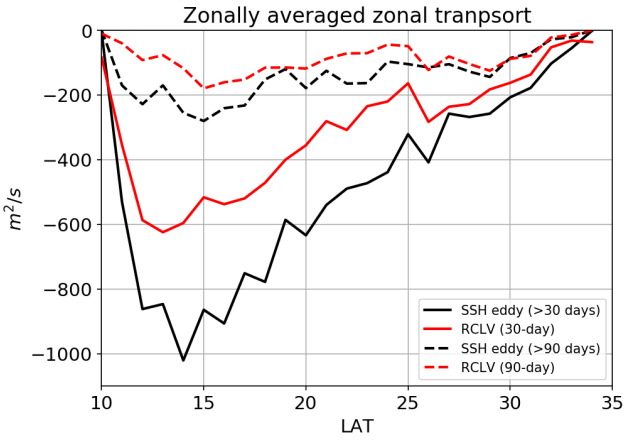

Figure 6. Zonally averaged zonal transport of RCLVs and SSH eddies (assuming SSH eddies could keep coherence).

$$\frac{d}{dt}\int_{\Omega}\phi dA = \int_{\Omega}\frac{\partial\phi}{\partial t}dA + \oint_{\partial\Omega}\phi\vec{u}\cdot\hat{n}dS = \int_{\Omega}(\frac{\partial\phi}{\partial t} + \vec{u}\cdot\nabla\phi)dA = 0. \tag{6}$$

In words, when the eddy boundary is a material boundary, the total amount of ϕ substance within the eddy is conserved, allowing the eddy to trap and translate its contents over large distances.

Generally, the velocity of Eulerian eddy boundaries (e.g. SSH contours in *Chelton et al.* [2011], PV contours in *Zhang et al.* [2014], and contours of the stream function field in *Nencioli et al.* [2010]) does not coincide with the fluid velocity because of the non-material detection method, which indicate the non-zero material flux across these boundaries. The question we address below is, *how much material leaks across the Eulerian eddy boundaries?*

4.2 Overlapping RCLVs and SSH eddies

The material flux across the eddy boundary can be understood as two processes: leakage and intrusion. Leakage means the initially inside water parcels escape into the background environment through the eddy boundary, and intrusion stands for the background water parcels entering into the eddy interior. Due to the practical difficulty of obtaining the eddy boundary velocity normal vector and conducting the integration along the curved boundary, we don't diagnose the material flux across the eddy boundary directly by (5). As a substitute, we approximate it via quantifying the number of Lagrangian moving across the eddy boundary. To do this, we employ the same Lagrangian particle experiments that were used to identify the RCLVs, described in the previous section.

In this section we consider the leakage across Eulerian eddies which overlap with RCLVs, 1973 eddies in total. For each eddy, the numbers of initially inside particles $N_{in}(t)$ and background particles $N_{out}(t)$ surrounded by SSH contour boundaries are calculated every day during the eddy lifetime. In addition, a normalized parameter describing the change of amplitude at the eddy center point is defined by, $SSHA_{norm} = (\eta_1 - \eta_0)/\overline{\eta(t)}$, where η_0, η_1, and $\overline{\eta(t)}$ represent initial, final, and mean amplitude over the eddy lifetime, respectively. Base on the $SSHA_{norm}$, these eddies are classified into three categories: growing eddy ($SSHA_{norm} > 0.25$), steady eddy ($-0.25 \leqslant SSHA_{norm} \leqslant 0.25$), and decaying eddy ($SSHA_{norm} < -0.25$). Each category accounts for about 30% of the overall sample, and the numbers are labeled in the legend of Figure 8.

Figure 7 depicts the processes of leakage and intrusion for three pairs of 30-day overlapping RCLVs and SSH eddies selected randomly, including the movement of particles and time series of particle numbers. The trends of SSH amplitude indicate they belong to growing eddy, decaying eddy,

and steady eddy, respectively. These three SSH eddies all move westward and contain a coherent core (RCLV) trapping initial water inside its boundary in 30 days. Unlike the coherent transport by RCLVs, part of the initial water inside the SSH eddies rapidly escapes from the eddy interior and joins in the background environment, then moves along with the local current. Simultaneously, the background water can intrude into SSH eddies. Among these three cases, the leakage ratio of the initial water reach about 20%, 33%, and 40%, respectively. The strongest intrusion occurs in the growing eddy, with about 34,000 Lagrangian particles from background flow intruding into it. This is because the eddy is expanding and more and more background water becomes enclosed by the outermost closed SSH contour. In contrast, the intrusion in the decaying eddy is relatively weak. To measure the rate of leakage and intrusion, the crossover point of leakage and intrusion trends is considered. The appearance of the crossover day means the volume of intruded water exceeds that of initial eddy water retained inside the SSH eddy. A quick (slow) crossover day corresponds to a strong (weak) material flux across boundaries. In this example, for both the growing and steady eddy, the crossover day is about 10th day. The decaying eddy, in contrast, has no crossover day because the intrusion is weak, due to the continuously decreasing eddy volume. Besides the coherent RCLV core, there appear to be some initial particles enclosed by SSH eddy boundaries, but not recognized as part of the Lagrangian coherent structure. The LAVD algorithm doesn't include this structure as part of RCLV, because it rotates differently from the main coherent core, existing in the form of filaments. A supplementary animation to show these three leaky SSH eddies is available at https://vimeo.com/341157321.

This material flux across SSH eddy boundaries from these random cases illustrates that the water surrounded by SSH contours at neighboring time isn't necessarily the same fluid. Since leaky part doesn't contribute to the coherent transport, the transport estimate based on SSH eddy boundaries may strongly overestimate the real coherent material transport, as represented by the RCLV core.

In the following statistical analysis, the leakage and intrusion are normalized by the initial particle numbers inside SSH eddies, which are given by $\frac{N_{in}(t)}{N_{in}^0}$ and $\frac{N_{out}(t)}{N_{out}^0}$, and their mean trends are described as $\overline{\frac{N_{in}(t)}{N_{in}^0}}$ and $\overline{\frac{N_{out}(t)}{N_{out}^0}}$. Figure 8 shows the normalized leakage trend and intrusion trend for all 30-day overlapping SSH eddies. The mean leakage ratio of all eddies is about 50%, which indicates roughly half of water initially enclosed by the SSH contour isn't coherently carried by the moving SSH eddy by the end of the detection period. The degree of leakage and intrusion for different categories of eddies are distinctive. Growing eddies and decaying eddies corresponds to weaker (40%) and stronger (60%) leakage of initial water, respectively. And the contrary trait is observed in the process of intrusion. The large mean value and standard deviation (red line and error bars in middle panel) for intrusion trend is from the growing eddy, whose normalized intruded particle number may be very large if the eddy area expands for several times than initial size. For steady eddies, the behavior of the leakage curve is close to that of growing eddies, with the leaky water accounting for about 40%. Besides the leaky part, the truly coherent structure (RCLV) accounts for about 25% of initially inside water, and its material boundary ensure the volume of this part of water remains constant during the lifetime (see dashed blue line in the right panel). The additional 25% or retained water evolves as a filament structure but still remain inside the SSH eddy boundary. The crossover time of averaged leakage and intrusion is 20 days.

We also estimate the material flux for the 359 longer-lived 90-day eddies. The results, shown in Figure 9, display similar behaviors to those of 30-day eddies, including the trends of leakage and intrusion for three categories of eddies. The average leakage ratio at the final time is about 50% as well. The crossover day of leakage and intrusion occurs on about 23th day. After the crossover day, the rate of leakage and intrusion become obviously slow, because mostly only the coherent core remains. Figure 10 shows histograms of the crossover day for 30- and 90-day SSH eddies. Grouped by eddy growth stage, for both shorter-lived and longer-lived eddies, the crossover day occurs in the sequence growing eddies, steady eddies, and decaying eddies. About 50% decaying 30-day eddies have no crossover day due to the weak intrusion. Distinct features are not observed when we group eddies as cyclonic and anticyclonic (not shown).

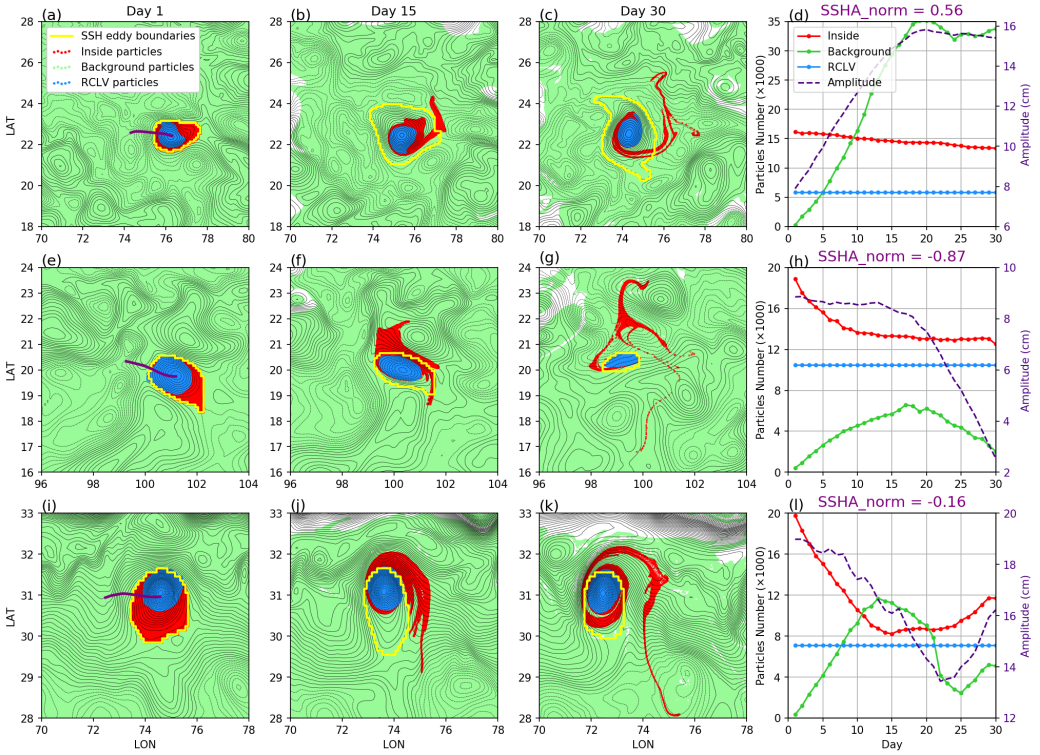

Figure 7. (the first three columns) The particle locations around three randomly selected overlapping eddies over 30 days. (fourth column) Time series of particle numbers for these three eddies. The growing eddy, the decaying eddy, and the steady eddy is shown in (a-d), (e-h), and (i-l), respectively. The red dots represent the initial particles inside SSH eddy boundaries (initial particles). The green dots represent the initial particles outside SSH boundaries (background particles). The blue dots indicate RCLVs particles. The yellow lines are SSH boundaries. The center points trajectories of SSH eddies are superimposed in purple lines. The normalized SSHA of three eddies are labeled in (d, h, and l).

4.3 Non-overlapping SSH eddies

The above examples give the impression that SSH eddies contain a coherent material core; however, we have so far only examined overlapping SSH and RCLV eddies. We now turn to the numerous non-overlapping SSH eddies, which account for roughly half of SSH eddy samples.

These SSH eddies can be detected by the SSHA contour method, but there is no Lagrangian coherent structure inside these SSH eddies. Thus we anticipate stronger exchange with the background. Figure 11 shows the movement of particles in 30 days around three randomly selected non-overlapping SSH eddies. For the growing eddy (top panels), after 30 days the SSH eddy is almost filled with intruded water, along with more than 90% initial water leaking out the boundary. Some particles still remain in the eddy interior for decaying eddy (middle panels) and steady eddy (bottom panels), but evidently these do not meet the requisite criteria for RCLV detection. The statistical results are shown in Figure 12. On average, the leakage for non-overlapping eddies reaches 60%, stronger than that of overlapping SSH eddies with a coherent core. In the same way, the intrusion process is also stronger compared to overlapping SSH eddies. And we note that the crossover day of leakage and intrusion is the 12th day, revealing that the material flux occurs at a faster rate.

Tightening the contour threshold will not enable non-overlapping SSH eddies keep the material coherence properties because of the strong leakage and intrusion process, which suggests that the

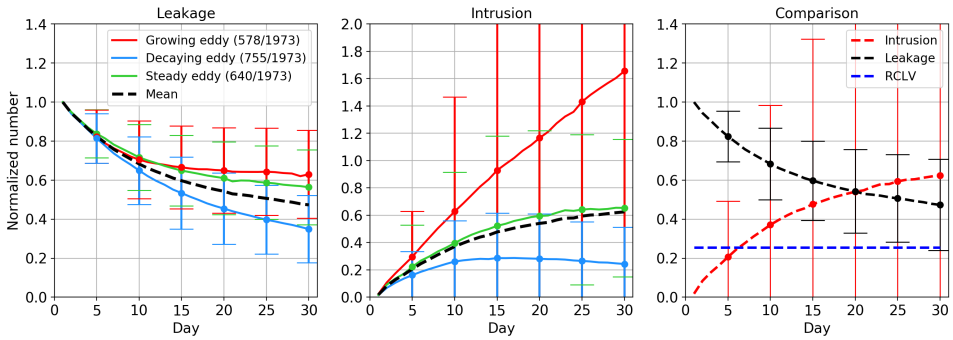

Figure 8. (left) Normalized leakage trend, (middle) intrusion trend, and (right) the comparison of leakage and intrusion for 30-day overlapping SSH eddies. The numbers of three categories of eddies are labeled in the legend in the left panel. The error bar indicates one standard deviation of the mean over all samples on that day. The invariable blue dashed line in the right panel indicates normalized RCLV particle number.

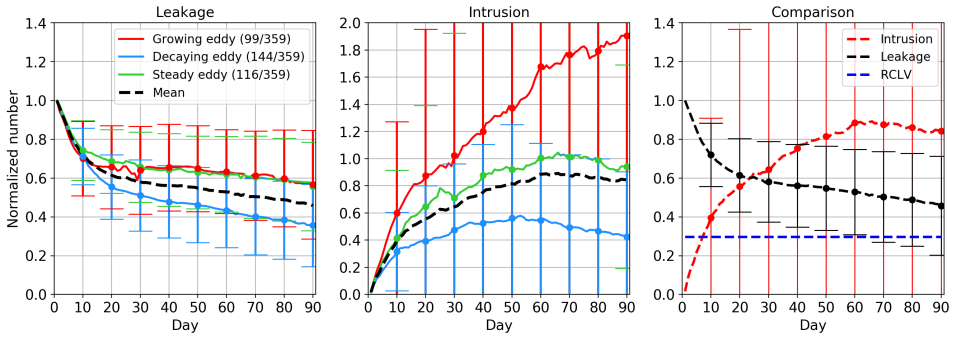

Figure 9. Same as Figure 8, but for 90-day overlapping eddies.

eddy coherence properties depend on whether the organization method is material, rather than the choice of thresholds or parameters. In other words, the water exchange across SSH eddy boundaries over the eddy whole lifetime shows the SSH eddies are far from materially coherent structures.

5 Random-Circle Eddy Model

The analysis above showed that the non-overlapping SSH eddies were significantly leakier than the ones that overlapped with RCLVs. But is there still some inherent material coherence to these SSH eddies that the RCLV detection algorithm fails to identify? In this section, we calculate the degree of leakage and intrusion around completely artificial eddies defined by randomly generated circles. This allows us to assess the differences in the material coherence properties between SSH eddies and arbitrary patches of water.

For a fair comparison, we generate a dataset of artificial eddies based on the statistical features of SSH eddies. The number distribution with radius of overlapping SSH eddies is displayed in Figure 14 (left), which suggests that more than 70% of overlapping SSH eddies range from about 50 km to 90 km in radius. Here, the SSH eddies with radius larger than 170 km are excluded because of their infrequent occurrence. Following this number and radius distribution, we structure the same amount of circles in the subtropical region for the following random eddy experiments. The initial locations of these circles are randomly selected in the subtropical basin during a random 90-day time interval. The random choice of the initial position and occurrence time distributes these 1969 circles roughly uniformly over the study region and time interval.

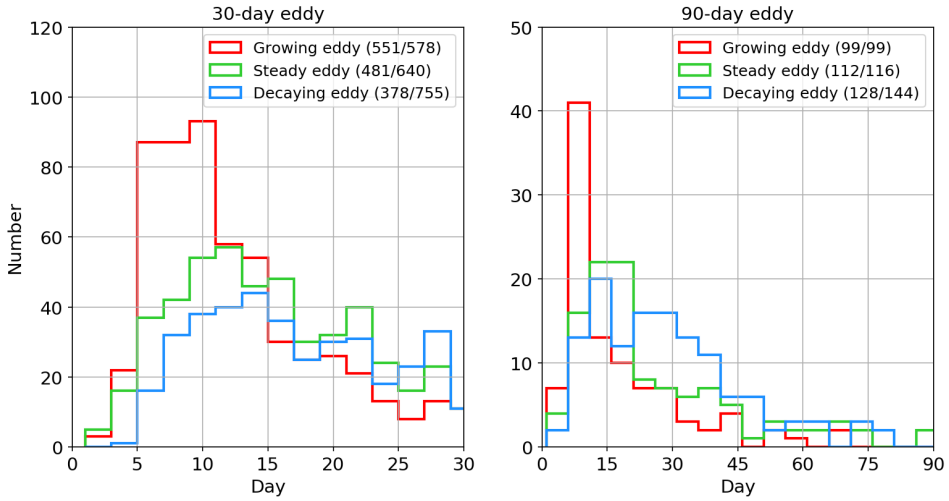

Figure 10. Histograms of the crossover day for (left) 30-day and (right) 90-day SSH eddies. Growing eddies, steady eddies, and decaying eddies are indicated by red, green, and blue lines, respectively. The total number of each group and the number of eddies with the crossover day are labeled in the legends.

We set up two simple scenarios for the random-circle eddy model. In scenario 1, the positions of the artificial circles are fixed at their initial positions. In scenario 2, these circles are advected by the mean velocity of the center point over 30 days. The radius of the random-circle remains constant for both two cases in the experiment, without the growth or decay of size. A quantification of leakage and intrusion across boundaries is conducted for the fixed-circle model and moving-circle model.

Figure 13 shows the process of material flux across artificial boundaries for two randomly selected circles from two different scenarios. For the fixed circle (top panels), which is initially overlaid on several closed SSH contours, the initial water parcels inside the circle boundary leak into the background flow in a fast rate, with the particle number decreasing above 80%, from about 19000 to about 3000 in 30 days. Figure 13 (a-c) shows that some initial particles surrounded by the boundary on the 30th day do not always remaine inside the circle, but rather reenter into the circle carried by an eddy-like structure after a quick leakage. For the moving circle (bottom panels), which propagates westward following the mean flow, about 30% initial particles remain after 30 days. The crossover time is 12 days, which indicate the leakage rate is slower comparing with the fixed case (7 days). These two cases suggest that, even though there is no the coherent structure, initial particles defined by artificial boundaries still have the possibility to remain inside these boundaries under effects of local background flow field.

Statistical results of normalized leakage and intrusion from fixed circles model and moving circles model are shown in Figure 14. After 30 days, there are about 18% and 32% initial water surrounded by these artificial boundaries for fixed and moving cases, respectively. The standard deviation of the intrusion for random-circles is close to that of the leakage, in contrast to the real SSH eddies. The reason is that the size of the random circle is constant, so there is no large normalization value of intrusion which is common in real eddies accompanying with the eddy size expansion. In particular, the leakage and intrusion trends of moving circles are quite similar to those of non-overlapping SSH eddies, and their crossover times are both 12 days.

Figure 15 displays the bar diagram for the ratio of leakage and intrusion after 30 days from 5 categories of eddies (circles), including RCLVs ,overlapping SSH eddies, non-overlapping SSH eddies, fixed circles, and moving circles. RCLVs by construction have no leakage and intrusion during the lifetime because their boundaries are material. Among the other 4 cases, the leakage in

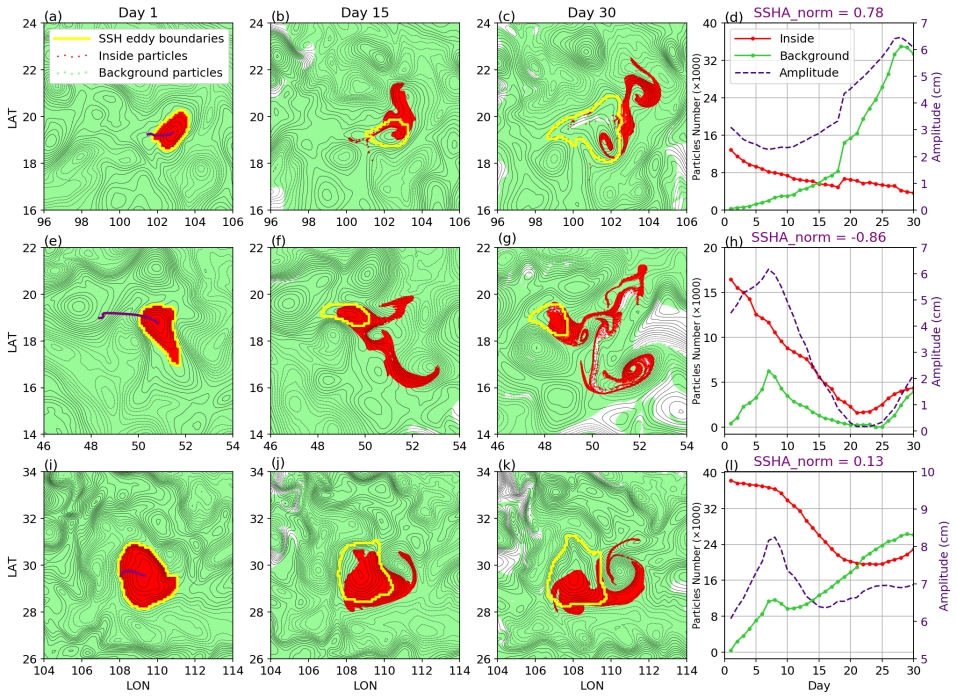

Figure 11. Same as Figure 7, but for three randomly selected non-overlapping SSH eddies. The top, middle, and bottom panels correspond to a growing eddy, a decaying eddy, and a steady eddy, respectively.

30 days for SSH eddies with the coherent core (overlapping SSH eddies) is the weakest, but it still exceeds 50% of initial water parcels.

These findings suggest that, though there is a slight difference in the magnitude of leakage and intrusion ratio, the material coherence properties of non-overlapping SSH eddies (about half of SSH eddy samples) are not significantly different from randomly selected pieces of ocean with the same size.

6 Discussion and Conclusions

Existing coherent eddy identification methods can be classified into two general categories: Eulerian (e.g., *Chelton et al.* [2011], *Nencioli et al.* [2010], *Faghmous et al.* [2015]) and Lagrangian (e.g., *Beron-Vera et al.* [2013], *Haller et al.* [2016]). A wealth of literature has reported some provocative results about coherent eddy transport based on Eulerian eddy boundaries, especially the surprising zonal eddy mass transport (30Sv) in *Zhang et al.* [2014]. However, several works (e.g. *Wang et al.* [2015], *Abernathey and Haller* [2018]) using Lagrangian frameworks indicate these Eulerian methods strongly overestimate the degree of eddy material transport. In this study, we explored the relationship between eddy detection methods and coherent material transport and quantitatively calculated the leakiness of Eulerian eddies.

An idealized eddy-resolving ocean basin, closely resembling the North Pacific ocean, was simulated using MITgcm. More than 55 million Lagrangian particles were introduced into the model and advected by 2D surface flow in the final 5 years. We identified Lagrangian coherent eddies (also called RCLVs) in 30- and 90-day intervals by the method *Haller et al.* [2016]. In the corresponding time interval, SSH eddies were detected from SSHA fields through the approach proposed by *Faghmous et al.* [2015].

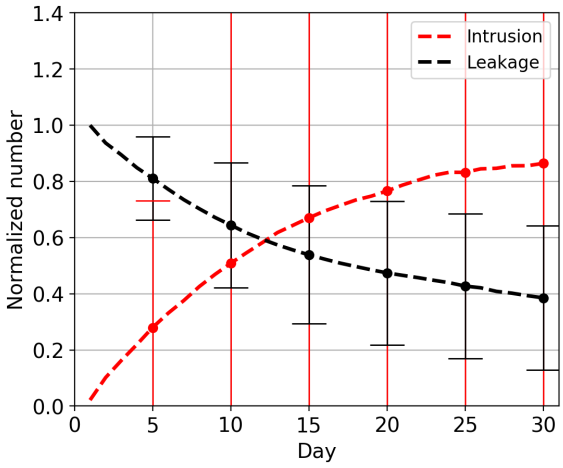

Figure 12. The averaged leakage and intrusion trend for non-overlapping SSH eddies in 30 days. The error bar indicates one standard deviation of the average over all eddies on the same day.

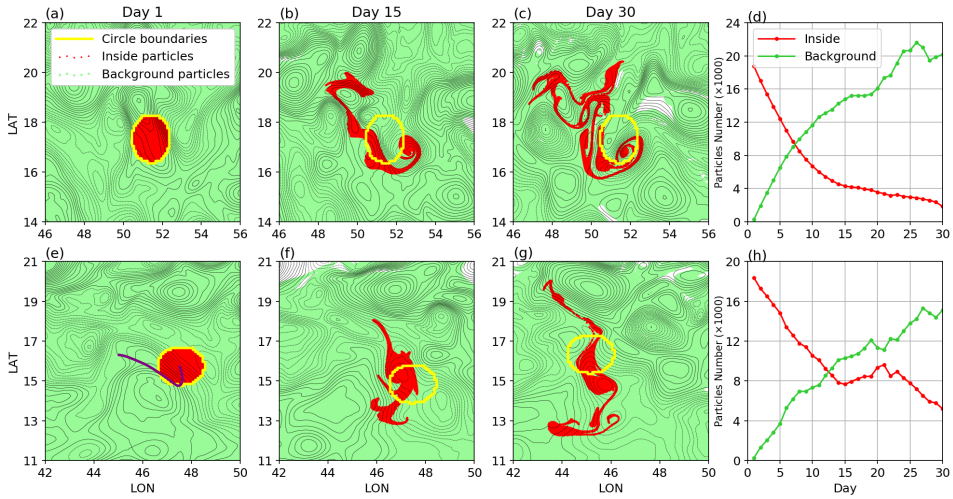

Figure 13. Same as Figure 7, but for randomly selected (top panels) a fixed circle and (bottom panels) a moving circle.

General statistical features of RCLVs were compared to those of SSH eddies. We found that RCLVs have a much smaller coherent core than SSH eddies and are often enclosed by SSHA contours. Specially, about 25% of RCLVs were found to be not located near a local peak of SSHA. We also found that mean radius of all RCLVs (35.5 km) is approximately about half of the mean SSH eddy radius (72.4 km). Both RCLVs and SSH eddies had similar westward propagation speeda with the latitude. Assuming SSH eddies could maintain coherence over their whole lifetimes, the zonal coherent transport by RCLVs was around half of the transport by SSH eddies.

The principal focus and innovation of this paper was the calculation of material flux across Eulerian eddy boundaries. The eddies were classified into three categories: overlapping RCLVs and SSH eddies, non-overlapping SSH eddies, and non-overlapping RCLVs. Using Lagrangian particles, we examined the processes of leakage and intrusion around overlapping and non-overlapping SSH eddies. For 30-day overlapping SSH eddies, over their lifetimes, the materially coherent part is only about 25% of the total volume (recognized as RCLVs), while about 50% of initial water escapes into

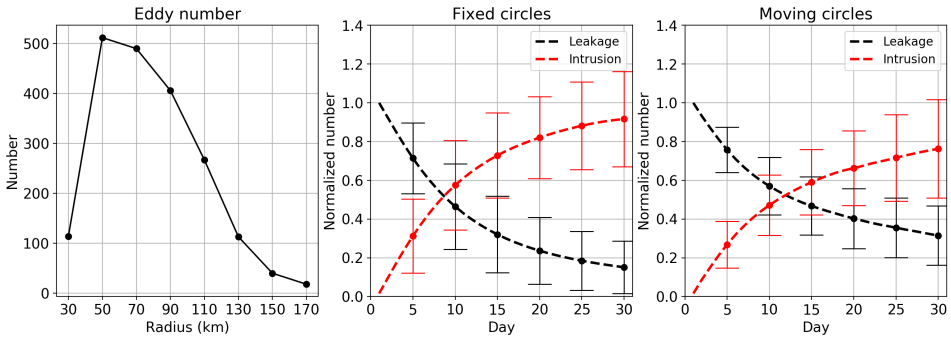

Figure 14. (left) The SSH eddy number distribution with radius. (middle and right) The averaged leakage and intrusion trend for randomly selected fixed and moving circles in 30 days. The error bar indicates one standard deviation of the average over all circles on the same day.

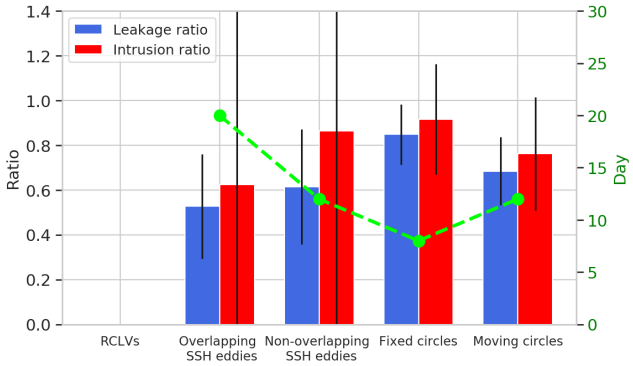

Figure 15. Bar diagram showing the ratio of leakage and intrusion after 30 days for RCLVs, overlapping SSH eddies, non-overlapping SSH eddies, fixed circles, and moving circles. The black error bar indicates the one standard deviation. The crossover day of leakage and intrusion is presented by the green dashed line. Specially, RCLVs have zero leakage and intrusion for their coherent property.

the background flow. The remaining 25% of water can still stay inside the SSH eddy boundary, but in the form of filaments outside the coherent core. After about 20 days, the intruded water exceeds the amount of initial water in SSH eddies, which provides an evidence that there is strong water exchange around SSH eddies. Strong leakage and intrusion are also found in 90-day overlapping SSH eddies. For non-overlapping SSH eddies, more water leakage (about 60%) occurs at a faster rate.

Following the number and radius of real SSH eddies, fixed circles and moving circles were selected in random regions and time interval to provide a baseline against which to compare the SSH eddies. After 30 days, there was still about 18% and 35% of initial water surrounded by these artificial boundaries for fixed and moving cases. In particular, the leakage and intrusion trends of moving circles were quite similar to that of non-overlapping SSH eddies. These findings suggests that the material coherence properties of roughly 50% of SSH eddies are not significantly different from randomly selected pieces of ocean with the same size.

The final conclusions from this study are clear: if one wishes to estimate material transport, a Lagrangian eddy detection algorithm is best, since Eulerian eddies are highly leaky. While Eulerian eddies may contain a materially coherent core, this core is identified well by the RCLV algorithm.

But there are just as many Eulerian eddies with no materially coherent core. We see no obvious way to separate these two cases *a priori*, i.e. without also doing Lagrangian eddy detection.

However, the fact is that running a model with millions of Lagrangian particles and conducting the identification remains a heavy computational task. The recent publication of an efficient Lagrangian Coherent Structure software package may mitigate this somewhat (`CoherentStructures.jl`; *Karrasch and Schilling* [2019]). We are also in the process of compiling a global RCLV database based on satellite altimetry, which should provide useful for future transport estimates.

Acknowledgments

Tongya Liu was supported by the National Natural Science Foundation of China (41730535, 41621064), the China Scholarship Council (NO. 201806320323). Ryan Abernathey was supported by NSF Award OCE 15-53593. The computation in this research is carried out on Habanero shared high perfomance cluster at Columiba Univerisity. The authors thank Wenda Zhang for the improvement of Lagrangian eddy detection algorithm, and Choe E. Tae for suggestions on this manuscript.

References

Abernathey, R., and G. Haller (2018), Transport by lagrangian vortices in the eastern pacific, *Journal of Physical Oceanography*, *48*(3), 667–685.

Beron-Vera, F. J., M. J. Olascoaga, and G. Goni (2008), Oceanic mesoscale eddies as revealed by lagrangian coherent structures, *Geophysical Research Letters*, *35*(12).

Beron-Vera, F. J., Y. Wang, M. J. Olascoaga, G. J. Goni, and G. Haller (2013), Objective detection of oceanic eddies and the agulhas leakage, *Journal of Physical Oceanography*, *43*(7), 1426–1438.

Beron-Vera, F. J., M. J. Olascoaga, G. Haller, M. Farazmand, J. Triñanes, and Y. Wang (2015), Dissipative inertial transport patterns near coherent lagrangian eddies in the ocean, *Chaos: An Interdisciplinary Journal of Nonlinear Science*, *25*(8), 087,412.

Cetina-Heredia, P., M. Roughan, E. Van Sebille, S. Keating, and G. B. Brassington (2019), Retention and leakage of water by mesoscale eddies in the east australian current system, *Journal of Geophysical Research: Oceans*, *124*(4), 2485–2500.

Chelton, D. B., R. A. Deszoeke, M. G. Schlax, K. El Naggar, and N. Siwertz (1998), Geographical variability of the first baroclinic rossby radius of deformation, *Journal of Physical Oceanography*, *28*(3), 433–460.

Chelton, D. B., M. G. Schlax, and R. M. Samelson (2011), Global observations of nonlinear mesoscale eddies, *Progress in oceanography*, *91*(2), 167–216.

Condie, S., and R. Condie (2016), Retention of plankton within ocean eddies, *Global Ecology and Biogeography*, *25*(10), 1264–1277.

Cox, M. D. (1985), An eddy resolving numerical model of the ventilated thermocline, *Journal of Physical Oceanography*, *15*(10), 1312–1324.

Dong, C., F. Nencioli, Y. Liu, and J. C. McWilliams (2011), An automated approach to detect oceanic eddies from satellite remotely sensed sea surface temperature data, *IEEE Geoscience and Remote Sensing Letters*, *8*(6), 1055–1059.

Dong, C., J. C. McWilliams, Y. Liu, and D. Chen (2014), Global heat and salt transports by eddy movement, *Nature communications*, *5*, 3294.

dÓvidio, F., J. Isern-Fontanet, C. López, E. Hernández-García, and E. García-Ladona (2009), Comparison between eulerian diagnostics and finite-size lyapunov exponents computed from altimetry in the algerian basin, *Deep Sea Research Part I: Oceanographic Research Papers*, *56*(1), 15–31.

Early, J. J., R. Samelson, and D. B. Chelton (2011), The evolution and propagation of quasigeostrophic ocean eddies, *Journal of Physical Oceanography*, *41*(8), 1535–1555.

Faghmous, J. H., I. Frenger, Y. Yao, R. Warmka, A. Lindell, and V. Kumar (2015), A daily global mesoscale ocean eddy dataset from satellite altimetry, *Scientific data*, *2*, 150,028.

Fox-Kemper, B., and D. Menemenlis (2008), Can large eddy simulation techniques improve mesoscale rich ocean models, *Ocean modeling in an eddying regime*, *177*, 319–337.

Frenger, I., M. Münnich, N. Gruber, and R. Knutti (2015), Southern o cean eddy phenomenology, *Journal of Geophysical Research: Oceans*, *120*(11), 7413–7449.

Froyland, G., C. Horenkamp, V. Rossi, and E. Van Sebille (2015), Studying an agulhas ring's long-term pathway and decay with finite-time coherent sets, *Chaos: An Interdisciplinary Journal of Nonlinear Science*, *25*(8), 083,119.

Fu, L.-L., D. B. Chelton, P.-Y. Le Traon, and R. Morrow (2010), Eddy dynamics from satellite altimetry, *Oceanography*, *23*(4), 14–25.

Gaube, P., D. B. Chelton, R. M. Samelson, M. G. Schlax, and L. W. OâĂŹNeill (2015), Satellite observations of mesoscale eddy-induced ekman pumping, *Journal of Physical Oceanography*, *45*(1), 104–132.

Griffies, S. M., M. Winton, W. G. Anderson, R. Benson, T. L. Delworth, C. O. Dufour, J. P. Dunne, P. Goddard, A. K. Morrison, A. Rosati, et al. (2015), Impacts on ocean heat from transient mesoscale eddies in a hierarchy of climate models, *Journal of Climate*, *28*(3), 952–977.

Hallberg, R. (2013), Using a resolution function to regulate parameterizations of oceanic mesoscale eddy effects, *Ocean Modelling*, *72*, 92–103.

Haller, G. (2005), An objective definition of a vortex, *Journal of fluid mechanics*, *525*, 1–26.

Haller, G. (2015), Lagrangian coherent structures, *Annual Review of Fluid Mechanics*, *47*, 137–162.

Haller, G., and F. J. Beron-Vera (2013), Coherent lagrangian vortices: The black holes of turbulence, *Journal of Fluid Mechanics*, *731*.

Haller, G., A. Hadjighasem, M. Farazmand, and F. Huhn (2016), Defining coherent vortices objectively from the vorticity, *Journal of Fluid Mechanics*, *795*, 136–173.

Hausmann, U., and A. Czaja (2012), The observed signature of mesoscale eddies in sea surface temperature and the associated heat transport, *Deep Sea Research Part I: Oceanographic Research Papers*, *70*, 60–72.

Isern-Fontanet, J., E. García-Ladona, and J. Font (2003), Identification of marine eddies from altimetric maps, *Journal of Atmospheric and Oceanic Technology*, *20*(5), 772–778.

Jayne, S. R., and J. Marotzke (2001), The dynamics of ocean heat transport variability, *Reviews of Geophysics*, *39*(3), 385–411.

Karrasch, D., and N. Schilling (2019), Fast and robust computation of coherent lagrangian vortices on very large two-dimensional domains, *arXiv preprint arXiv:1907.08449*.

Klocker, A., and D. P. Marshall (2014), Advection of baroclinic eddies by depth mean flow, *Geophysical Research Letters*, *41*(10), 3517–3521.

Kouketsu, S., H. Kaneko, T. Okunishi, K. Sasaoka, S. Itoh, R. Inoue, and H. Ueno (2016), Mesoscale eddy effects on temporal variability of surface chlorophyll a in the kuroshio extension, *Journal of oceanography*, *72*(3), 439–451.

Large, W. G., J. C. McWilliams, and S. C. Doney (1994), Oceanic vertical mixing: A review and a model with a nonlocal boundary layer parameterization, *Reviews of Geophysics*, *32*(4), 363–403.

Marshall, J., A. Adcroft, C. Hill, L. Perelman, and C. Heisey (1997a), A finite-volume, incompressible navier stokes model for studies of the ocean on parallel computers, *Journal of Geophysical Research: Oceans*, *102*(C3), 5753–5766.

Marshall, J., C. Hill, L. Perelman, and A. Adcroft (1997b), Hydrostatic, quasi-hydrostatic, and nonhydrostatic ocean modeling, *Journal of Geophysical Research: Oceans*, *102*(C3), 5733–5752.

Nencioli, F., C. Dong, T. Dickey, L. Washburn, and J. C. McWilliams (2010), A vector geometry–based eddy detection algorithm and its application to a high-resolution numerical model product and high-frequency radar surface velocities in the southern california bight, *Journal of Atmospheric and Oceanic Technology*, *27*(3), 564–579.

Okubo, A. (1970), Horizontal dispersion of floatable particles in the vicinity of velocity singularities such as convergences, in *Deep sea research and oceanographic abstracts*, vol. 17, pp. 445–454, Elsevier.

Peacock, T., G. Froyland, and G. Haller (2015), Introduction to focus issue: Objective detection of coherent structures.

Qiu, B., and S. Chen (2010), Interannual variability of the north pacific subtropical countercurrent and its associated mesoscale eddy field, *Journal of Physical Oceanography*, *40*(1), 213–225.

675 Reynolds, O., A. W. Brightmore, and W. H. Moorby (1903), *Papers on Mechanical and Physical*
676 *Subjects: The sub-mechanics of the universe*, vol. 3, The University Press.
677 Rio, M., S. Guinehut, and G. Larnicol (2011), New cnes-cls09 global mean dynamic topography
678 computed from the combination of grace data, altimetry, and in situ measurements, *Journal of*
679 *Geophysical Research: Oceans*, *116*(C7).
680 Risien, C. M., and D. B. Chelton (2008), A global climatology of surface wind and wind stress
681 fields from eight years of quikscat scatterometer data, *Journal of Physical Oceanography*, *38*(11),
682 2379–2413.
683 Sinha, A., D. Balwada, N. Tarshish, and R. Abernathey (2019), Modulation of lateral transport by
684 submesoscale flows and inertia-gravity waves, *Journal of Advances in Modeling Earth Systems*,
685 *11*(4), 1039–1065.
686 Tarshish, N., R. Abernathey, C. Zhang, C. O. Dufour, I. Frenger, and S. M. Griffies (2018), Identifying
687 lagrangian coherent vortices in a mesoscale ocean model, *Ocean Modelling*, *130*, 15–28.
688 Wang, Y., M. J. Olascoaga, and F. J. Beron-Vera (2015), Coherent water transport across the south
689 atlantic, *Geophysical Research Letters*, *42*(10), 4072–4079.
690 Wang, Y., F. J. Beron-Vera, and M. J. Olascoaga (2016), The life cycle of a coherent lagrangian
691 agulhas ring, *Journal of Geophysical Research: Oceans*, *121*(6), 3944–3954.
692 Weiss, J. (1991), The dynamics of enstrophy transfer in two-dimensional hydrodynamics, *Physica*
693 *D: Nonlinear Phenomena*, *48*(2-3), 273–294.
694 Zhang, Z., W. Wang, and B. Qiu (2014), Oceanic mass transport by mesoscale eddies, *Science*,
695 *345*(6194), 322–324.